Simulation of air bubble scattering effects in 193 nm immersion interferometric lithography

C. H. Lin
National Nano Device Laboratories, No. 26, Prosperity Road I, Science-Based Industrial Park, Hsinchu, Taiwan, Republic of China

L. A. Wang[a)]
Department of Electrical Engineering and Institute of Electro-Optical Engineering, National Taiwan University, Taipei, Taiwan, Republic of China

(Received 1 June 2005; accepted 13 October 2005; published 1 December 2005)

In 193 nm immersion lithography, the presence of air bubbles in water poses a serious concern to the resist image formation. In this study, air bubble scattering effects were characterized by the Mie theory and the finite-difference time-domain (FDTD) method. The influence range of bubbles both in forward and lateral directions with respect to their sizes was analyzed. It is predicted that as bubble size exceeds 90 nm in diameter, light scattering becomes significant. In the FDTD simulation, the effects of scattered waves in two- and three-beam interferometric lithography were simulated to mimic the actual imaging formation in an immersion scanner. It is found that the more beams are involved in the image formation, the more scattered waves interfere with the image forming waves, and then degrade the final image. Finally, the effect of a moving bubble was also simulated. The phenomenon of image distortion in the presence of bubbles was simulated by employing the three-dimensional FDTD method. © *2005 American Vacuum Society.*
[DOI: 10.1116/1.2134716]

I. INTRODUCTION

ArF-laser based immersion photolithography has been considered recently as a potential "next generation lithography" for optical imaging at 45 nm device nodes and possibly beyond.[1] Since it evolves from the conventional mainstream optical technology and enables the extension of utilizing most existing facility, it has attracted much attention recently.[2,3] So far water has been considered as the most ideal immersion medium to fill the image space, i.e., space between the last lens element and the wafer. One of the issues in immersion lithography is the effect of air bubbles which can be generated from the disturbance of various sources such as pressure, temperature, photochemical reaction, fluid dynamics, and so on. Several works regarding to the bubble's effects have been reported.[4–6] In Switkes' work, various scattering sources were discussed, including the intrinsic scatter of water molecules, microbubbles arose from the devolution of dissolved gas, and photoinduced outgassing from resists, and nanobubbles coming from the hydrophobic resist surface.[5] It was also reported that bubble induced defect were the unique defect type appearing on the immersions wafers. Circular signatures of absent pattern regions indicated that microbubbles were the cause.[7] Therefore, it is important to identify to what extent the scattering effects, owing to bubble size and its relative position to the imaging plane (i.e., resist on a wafer), become significant.

Previously, we built immersion interferometric lithographic systems for experimental exploration, and some results were reported.[8] In this article, the minimal bubble size that can exist in water was analyzed. The Mie theory was used to analyze the scattering effects of various bubble sizes analytically. The influence range of different bubble size was also presented. The finite-difference time-domain (FDTD) method was used to simulate the interaction of the scattered waves and the image forming light numerically. The scattering effects of moving bubbles were also taken into account.

II. ANALYSIS OF THE MINIMAL BUBBLE SIZE THAT CAN EXIST IN AN IMMERSION LITHOGRAPHIC TOOL

Bubble size is one of the determinants affecting the imaging quality when the immersion lithography is employed. We first find out the minimal bubble size that can exist in an immersion lithographic tool, and then explore the size range of bubble beyond which light scattering effects cannot be ignored.

Assume a bubble is in the form of a sphere and in a steady state as shown in Fig. 1. At the mechanical equilibrium, the following relationship holds:

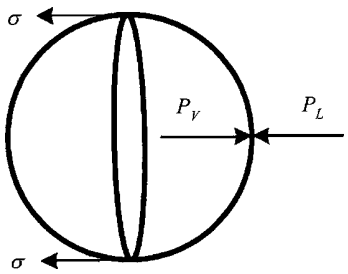

FIG. 1. Steady spherical bubble with the exerted forces.

[a)]Electronic mail: lon@ntu.edu.tw

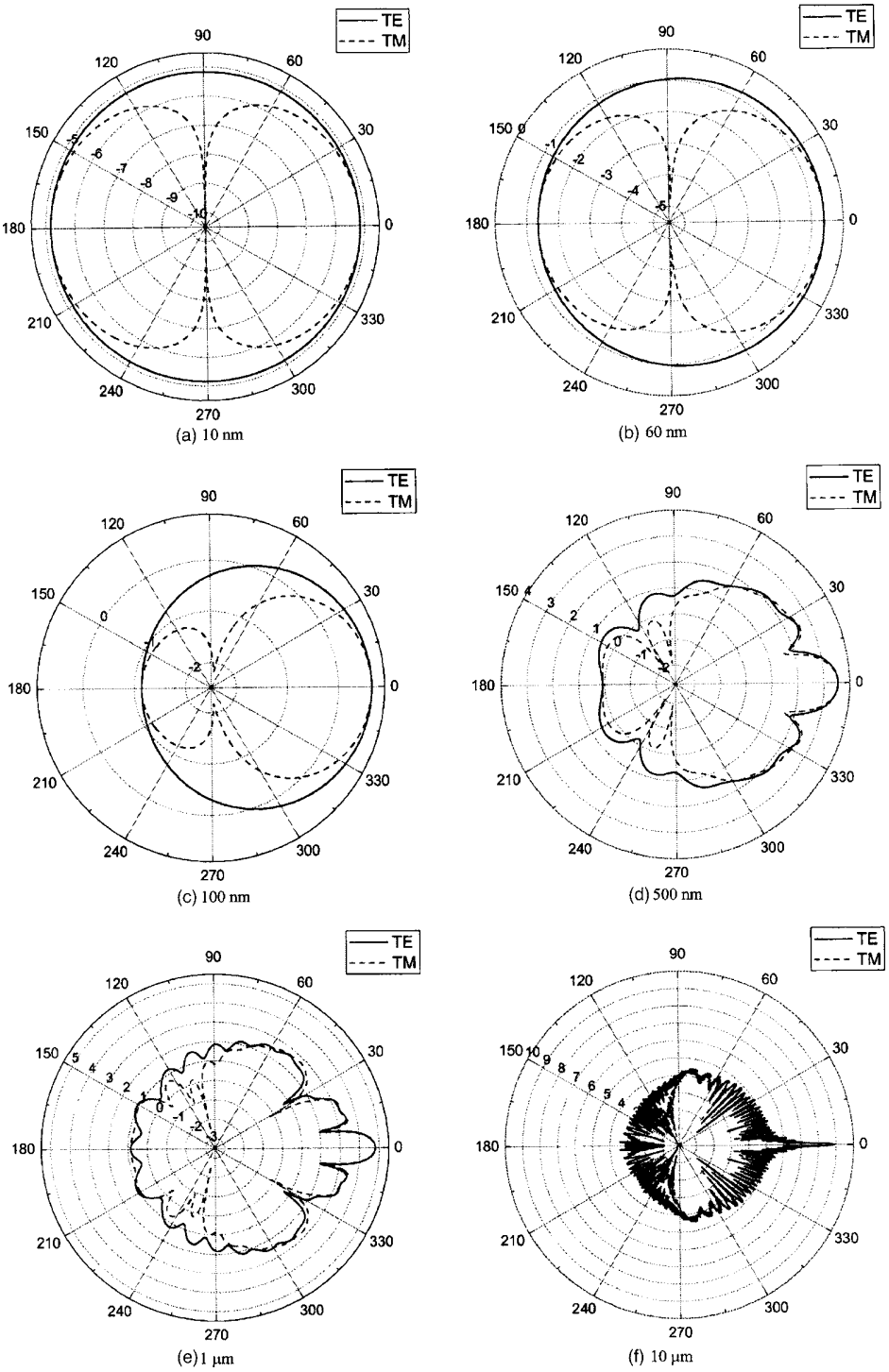

FIG. 2. Scattering spectra of air bubbles having size of (a) 10, (b) 60, (c) 100, (d) 500 nm, (e) 1, and (f) 10 μm in diameter. The magnitude is based on log scale.

$$(P_V - P_L) \times \pi r^2 = \sigma \times 2\pi r, \tag{1}$$

where P_L is the external pressure from liquid and atmosphere, P_V internal pressure of bubble, and σ the surface tension of liquid which has a value of 7.5×10^{-2} N/m^2 for water.

The radius of a bubble can then be expressed as

$$r = \frac{2\sigma}{P_V - P_L}. \tag{2}$$

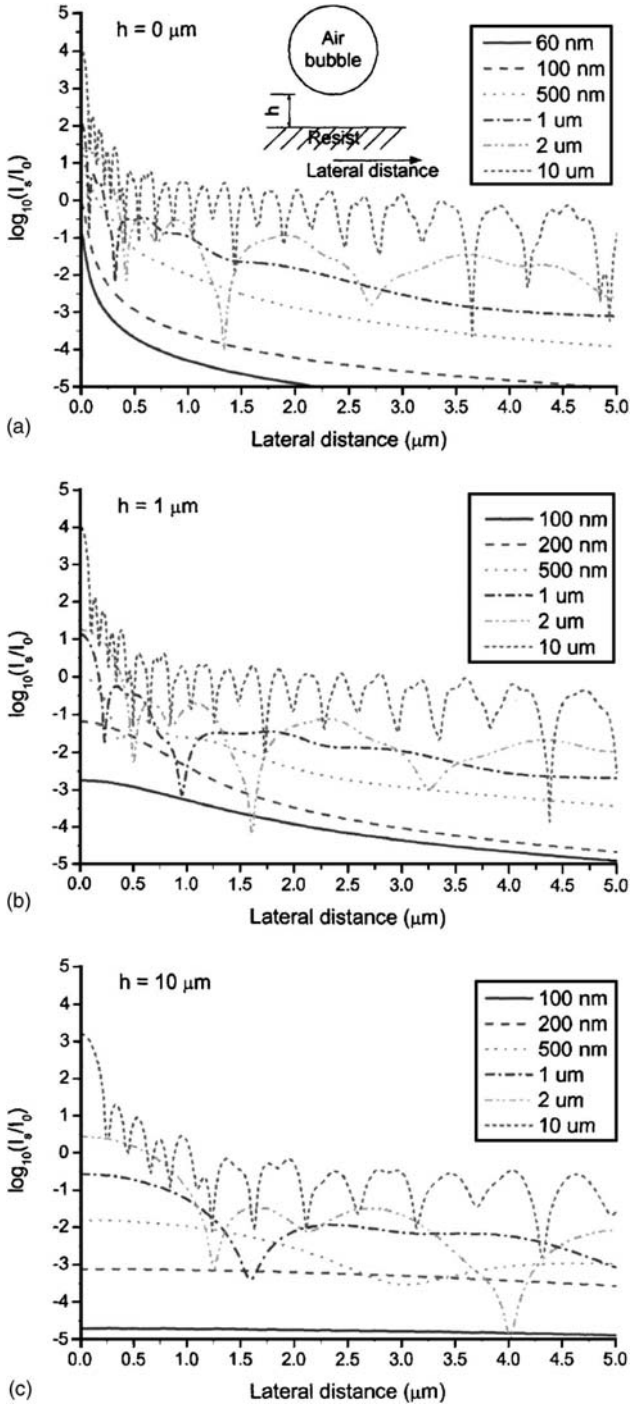

FIG. 3. Scattered intensity of bubbles with various sizes at the distance of (a) 0, (b) 1, and (c) 10 μm from the resist surface.

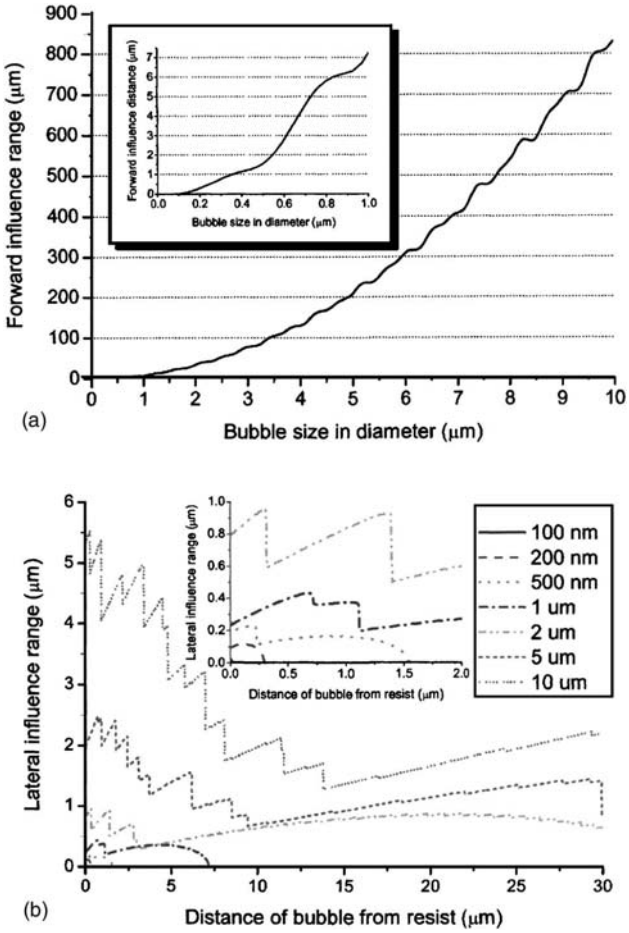

FIG. 4. (a) Influence range of bubbles in the forward direction. (b) The lateral influence range of bubbles with respect to their distance from the resist.

Typically the water depth is only a few centimeters for an exposure system to be used in immersion lithography. P_L can be assumed constant, approximately one atmospheric pressure, and can be neglected as compared with P_V. The bubble radius is then inversely proportional to P_V. Also, it suffices to say that the critical pressure of H_2O gas is 218 atm.[9] Therefore, once P_V is larger than 218 atm or 220.8×10^5 N/m^2, water has no liquid phase. The bubble would be unstable, and the water molecules around the bubble would also be unstable. Under the circumstances, the minimal bubble size that can exist is found to be $\sim$7 nm, which falls in the range from 1.2 to 18 nm calculated for the minimal homogeneous bubble nuclear size by using Gibbs energy.[10]

III. MIE ANALYSIS OF AIR BUBBLE EFFECT

When light encounters a bubble, absorption and scattering occur. We applied the Mie theory[11] to calculate the scattering spectra of air bubbles in water. The scattered field amplitudes can be obtained from

$$\begin{bmatrix} E_{\perp s} \\ E_{\| s} \end{bmatrix} = \frac{e^{ikr}}{r}\frac{i}{k}\begin{bmatrix} S_1(\cos\theta) & 0 \\ 0 & S_2(\cos\theta) \end{bmatrix}\begin{bmatrix} E_{\perp 0} \\ E_{\| 0} \end{bmatrix}, \tag{3}$$

where $E_{\perp 0}$, $E_{\perp s}$ are the incident/scattered fields perpendicular to the scattering plane (TE); $E_{\|0}$, $E_{\|s}$ are the incident/scattered fields parallel to the scattering plane (TM); S_1, S_2 are the scattering amplitudes evaluated from Mie series; θ is the scattering angle (0° for forward scattering, 180° for backward scattering); and r is the distance from the scattering sphere and $k=2\pi n/\lambda$, n is the refractive index of the medium surrounding the scattering sphere.

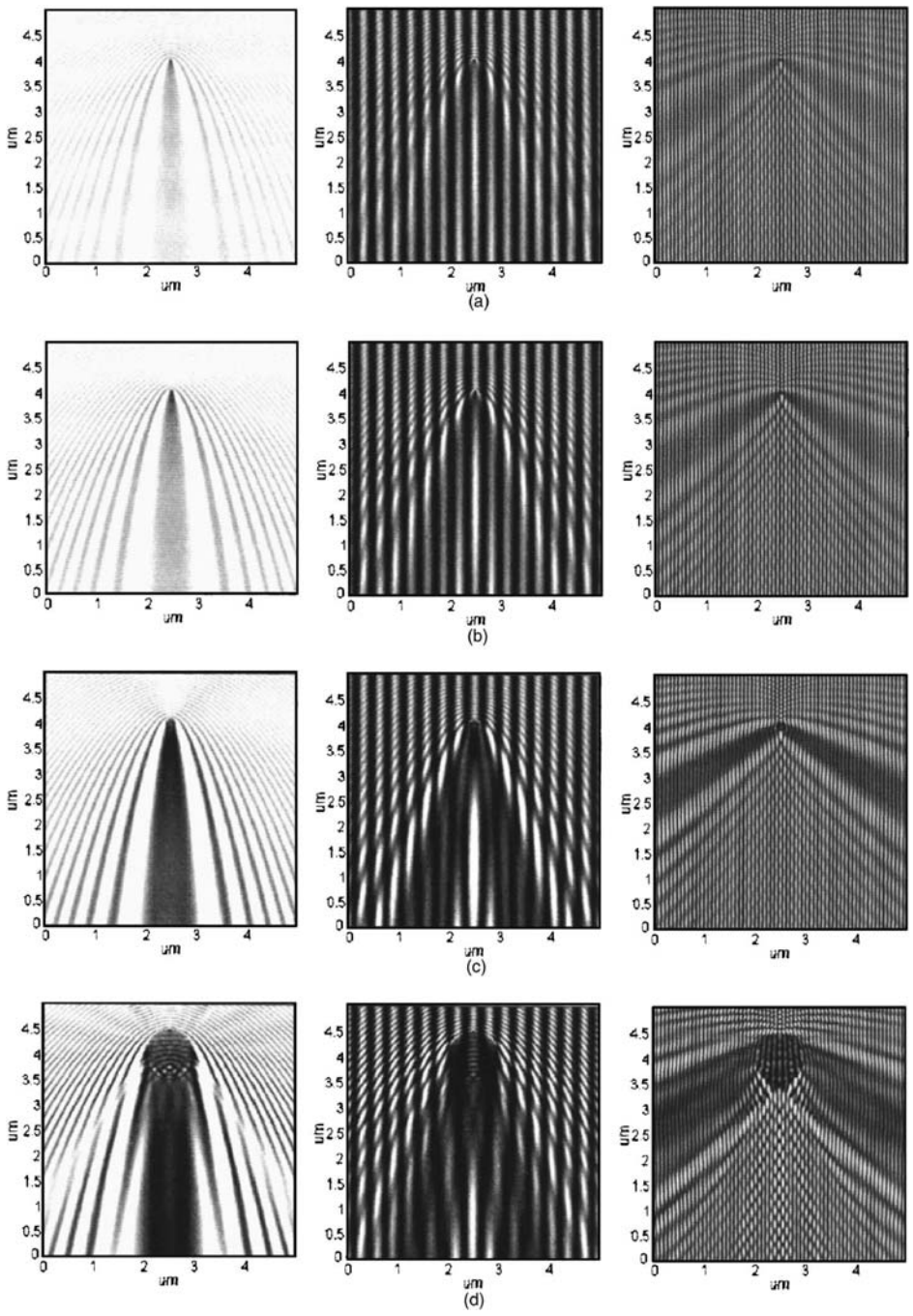

FIG. 5. Near field scattering effect of one air bubble having size of (a) 60, (b) 90, (c) 200 nm, and (d) 1 μm in diameter with one beam illumination (left column), two beams interference under TE polarization. The incident angles are 12° (center column, grating period $\Lambda \approx 323$ nm) and 60° (right column, $\Lambda \approx 77.5$ nm), respectively.

As shown in Fig. 2, scattering spectra of air bubbles ranging from 10 nm to 10 μm in diameter are drawn in polar plots. The smaller the bubble is, the variation of scattering intensity with angle becomes smaller. Here, we focus on TE polarization since the TE polarized light is preferred in interference. As seen from Fig. 2(a), bubbles smaller than 10 nm essentially do not generate any defects because they fall in Rayleigh scattering regime and have isotropic intensity distribution. In the range from 10 to 60 nm, the intensity of the scattered waves is very small as compared with the intensity of incident light and is significant enough to develop patterns. Note all these figures are based on log scale, and two adjacent circles mark a ten-time intensity difference. As the bubbles become larger, more scattered light falls in the forward direction.

To see the effects of the scattered light on the resist surface, the scattered intensity of air bubbles at the distance of 0, 1, and 10 μm from the resist surface is further calculated

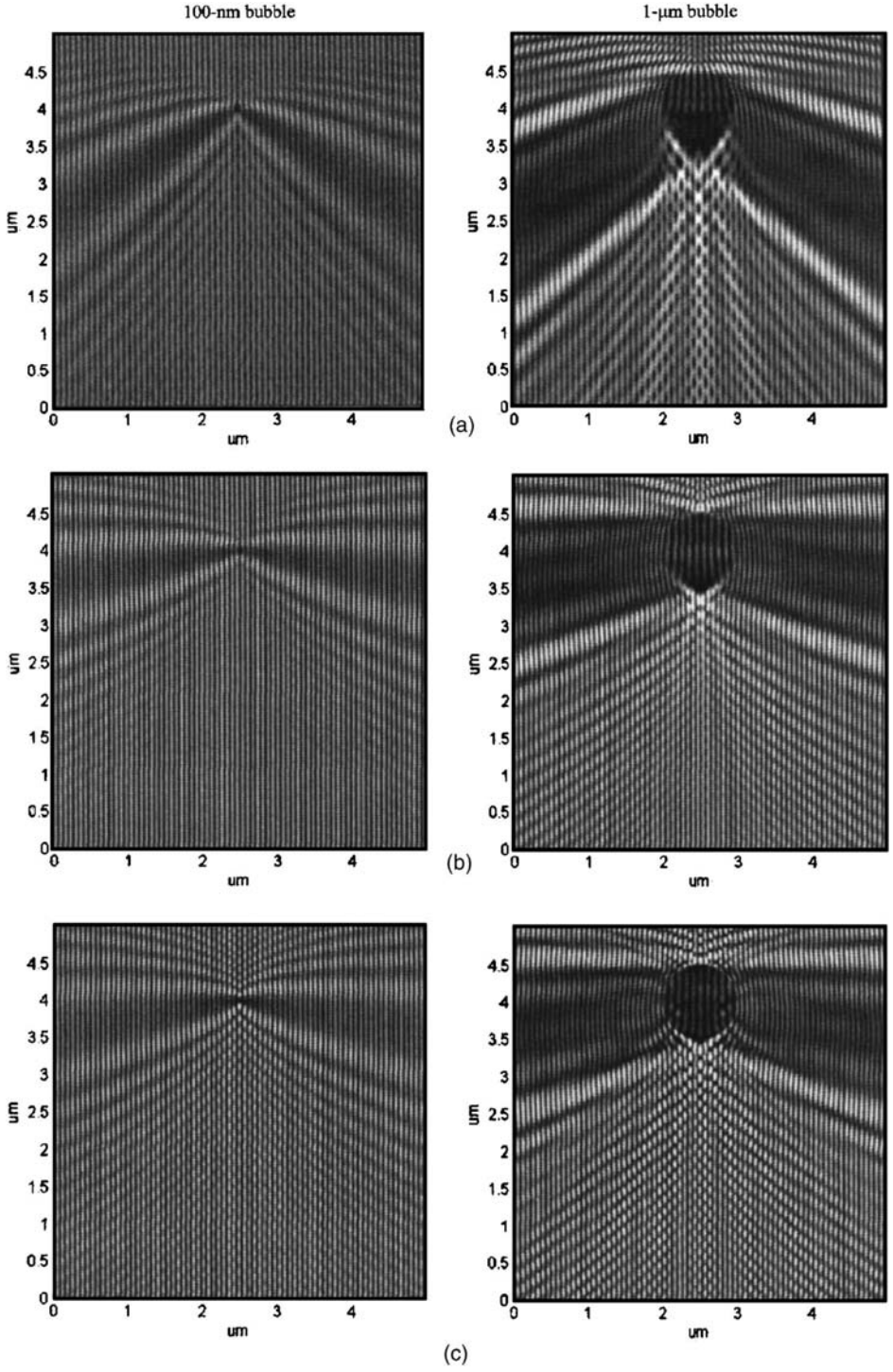

FIG. 6. Near field scattering effect of one air bubble having size of 100 nm (left column) (b) 1 μm (right column) in diameter under (a) 60° TM, (b) 80° TM, and (c) 80° TE two-beam interference.

and shown in Fig. 3. For nanobubbles ranging from 100 nm and smaller than 500 nm, the scattered light in forward direction can play a significant role on affecting the image formation. The shadow arose from the nanobubbles could be found in the resulting image when the bubbles were just sitting on the resist surface. As the observation point is moving away from the bubbles both in forward and lateral direction, the scattered light is decayed rapidly due to the $1/r^2$ term of the radiation field from the scattering sphere.

For microsize bubbles, the scattered light in forward direction is strong. Bubbles getting closer to the resist surface have stronger impact on the image. The bubble will behave as an obstacle in the optical path and therefore form a shadow image beneath the bubble. Furthermore, the variation

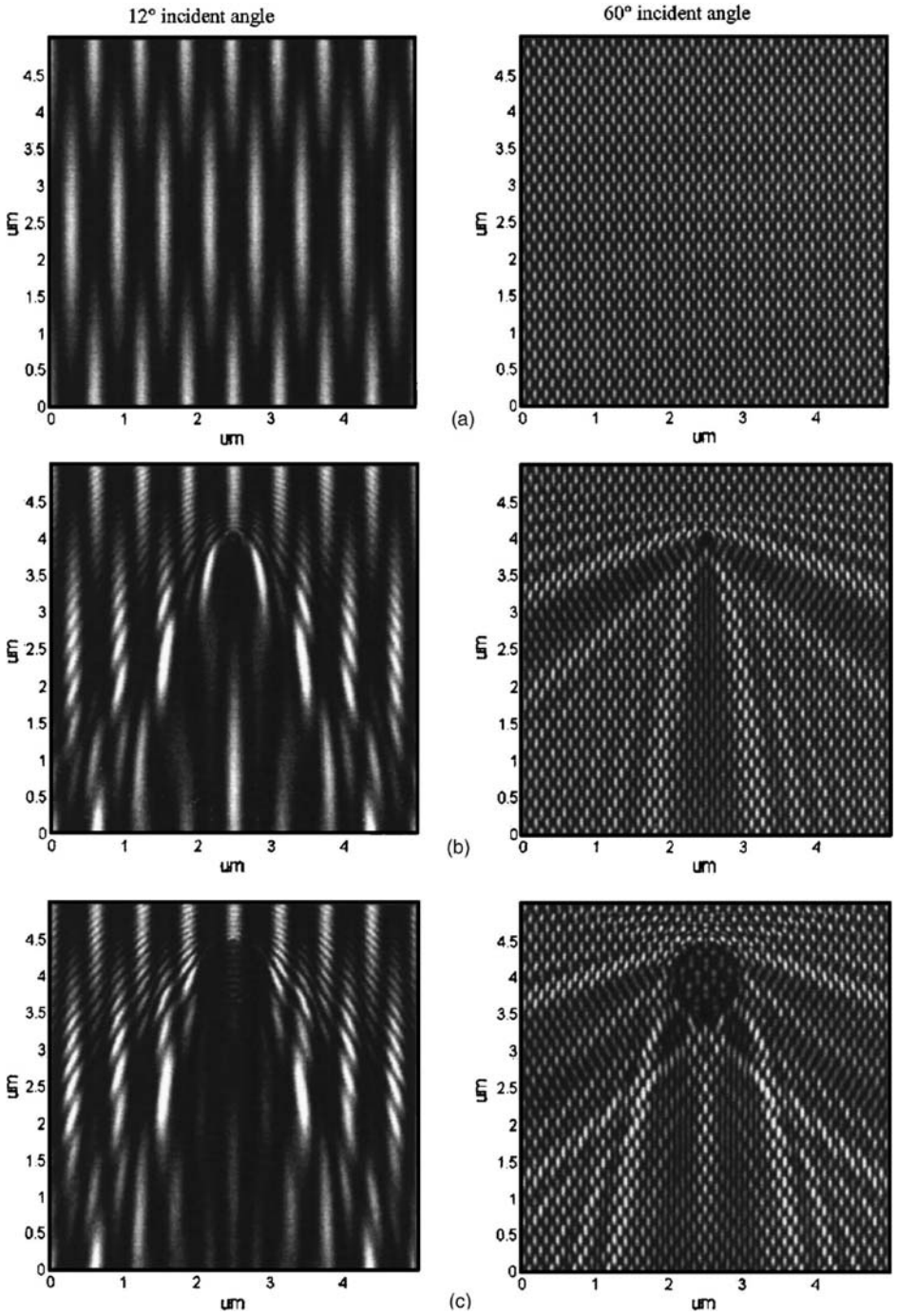

FIG. 7. FDTD calculations of three-beam interference with (a) no bubble, (b) 200 nm size bubble, and (c) 1 μm size bubble under TE illumination. Incident angle of 12° is shown in the left column and 60° in the right column.

of scattered fringes from the bubble in the lateral direction is large. The interference between the scattered light and image forming light will deform the resulting image around the microbubble.

In the following calculation, when the ratio of scattered/incident light, I_s/I_0, is larger than 0.5 we assume defects will incur on a resist, and over which distance the influence range is defined. To show the variation of the influence range with bubble size, Eq. (3) is further expressed as

$$r = \frac{1}{\sqrt{I_s/I_0}} \frac{|S_1(\cos\theta)|}{k}. \tag{4}$$

The influence range of bubbles in the forward direction with respect to their size is plotted in Fig. 4(a). From the calculated results, bubbles with the size starting from 88 nm will give their impact on the image. Bubbles of 1 μm can have their scattering effects over 7 μm in the forward direction. The propagation of light wave in water is assumed to be

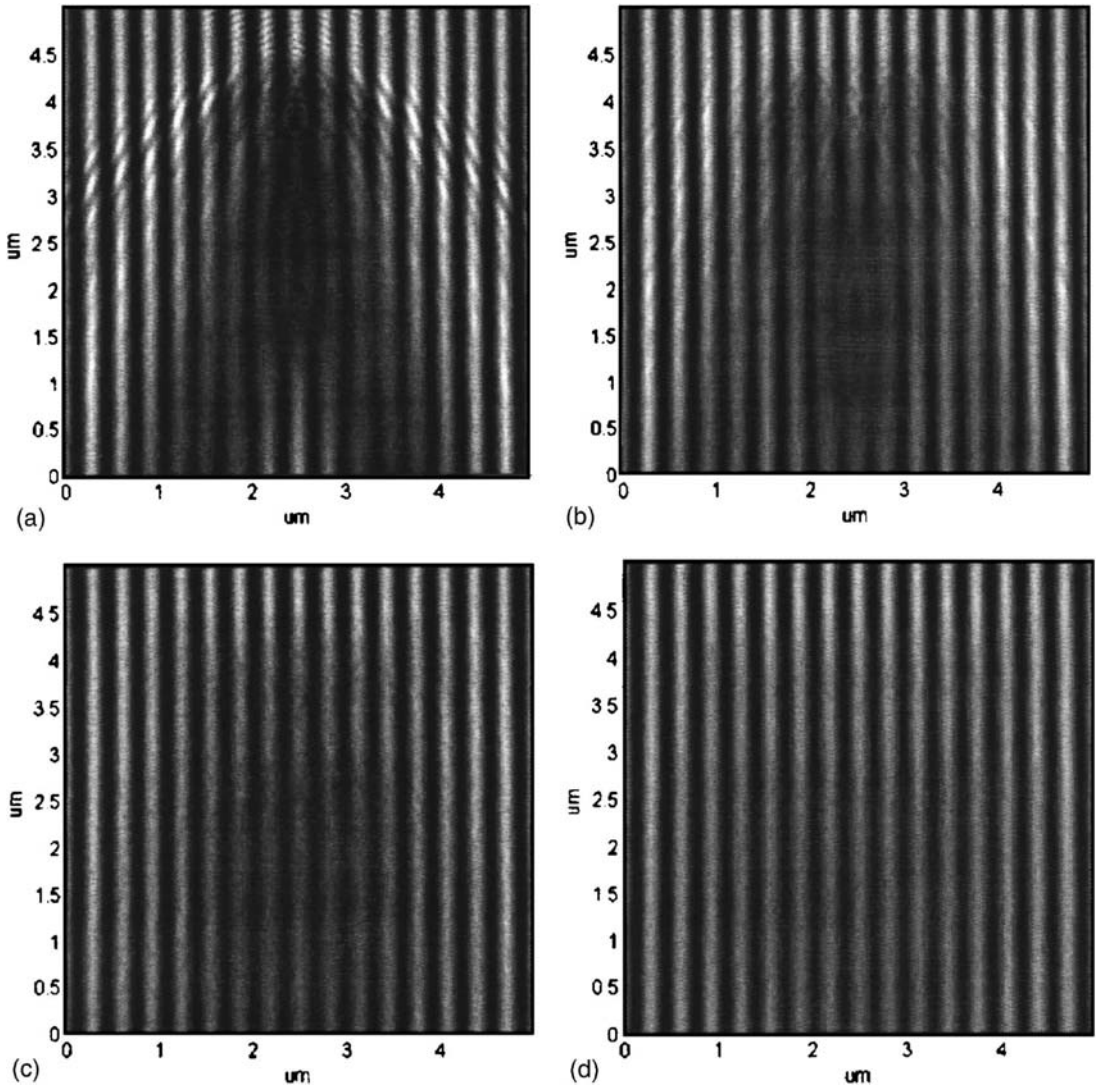

FIG. 8. FDTD simulation of 1 μm size moving bubble with a given speed of (a) 40, (b) 80, (c) 120, and (d) 160 μm/s under two beam TE illumination. The incident angle is 12°.

lossless here. For larger bubbles, their influence range in the forward direction will be much more longer.

Moreover, Fig. 4(b) shows the lateral influence range of bubbles with respect to their distance from the resist. The suddenly drops in the lateral influence range is due to the shift of the scattered fringe to the inner scattered fringe when the bubble is getting away from the resist surface. For the bubble size around 100 nm, the influence of the scattering effect is localized and will incur defects only when the bubble is directly attached to the resist surface. As the bubble size is getting larger, the influence of the scattered waves tends to go deeper in the forward direction rather than to spread wider in the lateral direction.

IV. FDTD SIMULATION

In the earlier Mie analysis, the calculations focus on the intensity field of the scattered light from the scattering sphere. It is difficult to calculate the coherently interfered electrical field between scattered waves and image forming wave by using the Mie theory. To calculate the scattering in such case, it is better to use the following FDTD numerical approach instead.

The FDTD method discretizes Maxwell's equations in space and time in a straightforward manner and serves as a tool of visualization of tracking the time-varying fields throughout the space of interest. Here we use the FDTD method to simulate the light propagation under the influence of a bubble. A perfect matched layer method is adopted for the absorbed boundary condition with the total/scattered field technique to handle the plane wave boundary.[12] In the following, we show the calculated light intensity distribution of the plane encompassing the diameter of the spherical bubble. When a plane wave is incident upon the water-air interface, its propagation direction may change owing to refraction and total internal reflection.

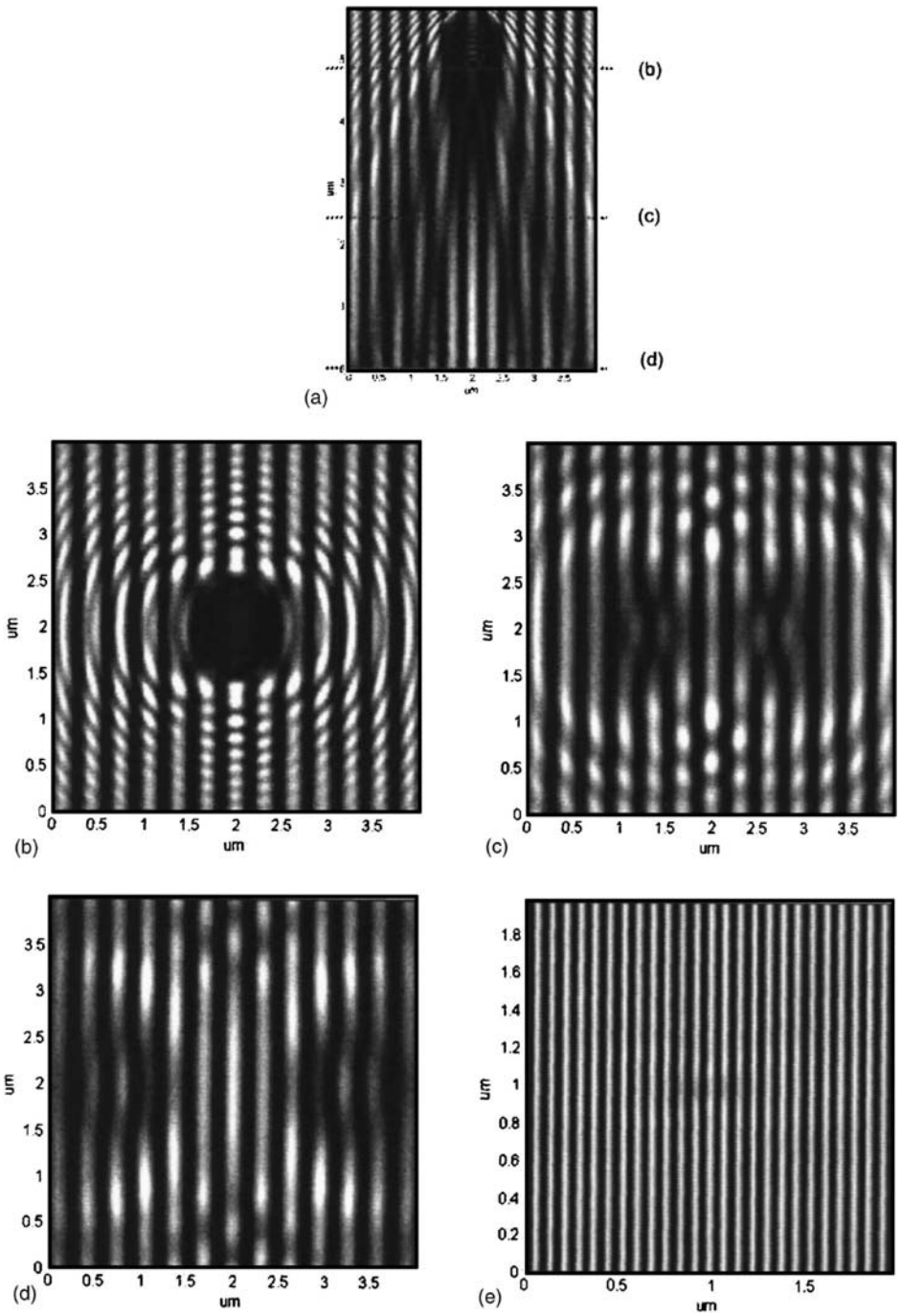

FIG. 9. 3D-FDTD simulation on the scattering effects. (a) The cross-section intensity distribution of a 1 μm bubble under TE-polarized two-beam illumination with an incident angle of 12° and its corresponding images taken (b) 0, (c) 2.4, and (d) 4.8 μm farther away from the bubbles. (e) The image tangential to the last surface of a 60 nm bubble under TE-polarized two-beam illumination with an incident angle of 60°.

A. Near field scattering effect of an air bubble

Near field scattering effects of one air bubble were evaluated by two-dimensional (2D) FDTD simulation under TE polarized illumination as shown in Fig. 5. Bubbles of different sizes ranging from 60, 90, 200 nm, and 1 μm in diameter were simulated. The left column of Fig. 5 shows the scattering effects under one plane wave illumination. The cases of two-beam interference were also considered to observe the scattering effects on image formation. Two incident angles are illustrated, one is 12° forming a grating period of 323 nm (shown in the middle column of Fig. 5) and the other is 60° forming a grating period of 77.5 nm (shown in the right column of Fig. 5).

For interference with two equal intensity beams, the resultant intensity of TE and TM can be expressed as

$$I_{\mathrm{TE}}(x) = 2I_0[1 + \cos(2kx \sin\theta)],$$

$$I_{\mathrm{TM}}(x) = 2I_0[1 + \cos(2kx \sin\theta)\cos(2\theta)], \quad (5)$$

where I_0 is the intensity of each beam, θ is the incident angle, and k is the amplitude of wave vector. In all the following two-beam simulation, a simple resist model with a constant threshold of $2I_0$ was applied to clarify the influence of bubble scattering effects.

As shown in Fig. 5(a), the scattering fringe from a 60 nm size bubble is not apparent under one beam illumination and its intensity variation is small as the wave propagates farther away from the bubble. For a 90 nm bubble, as shown in Fig. 5(b), defects can be clearly resulted if the bubble is adhered to the resist surface. As the wave propagates farther away from the bubble, light scattering effects become less significant in this case. Together with the results from the Mie theory, we can conclude that the scattering comes to affect the image when the bubble size is getting larger than 90 nm. As the bubble size becomes comparable with the illuminating wavelength or even larger, as shown in Figs. 5(c) and 5(d) for the bubble sizes of 200 nm and 1 μm, the scattering effects are clearly seen and cannot be ignored.

B. Polarization effect

The scattering effects of TM polarization were also evaluated in this study. In Fig. 6(a), scattering effects of a 100 nm and a 1 μm bubble were simulated under two-TM-beam interference with an incident angle of 60°. As compared with the right column of Figs. 5(b) and 5(d), the intensity contrast of TM polarization is apparently lower than that of TE polarization because of the $\cos(2\theta)$ factor of the TM interference, where θ is the incident angle. Figures 6(b) and 6(c) show the scattering results with 80° incident angle under TM and TE illumination. It is interesting to note that the TM scattering phenomenon of near the optical axis is better than TE scattering. This confirm with the results calculated by Mie theory. As compared with the Mie spectra in Fig. 2, the scattered intensity of TM is relatively smaller when the scattering angle is large.

C. Three-beam interference

In optical lithography, light transmitting through a mask carries all spatial frequencies of the mask. Such spatial frequencies can be viewed as the superposition of the plane waves with different incident angles. An optical system which is used to collect all these waves to form the desired image can be regarded as a low-pass filter. The 0th and ±1st orders are sufficient to mimic such imaging formation. Therefore, a simple three-beam interference is included to simulate the influence of the bubble scattering effects on image formation. For TE polarization, the resultant intensity can be described as

$$I = |\vec{E}_0 + \vec{E}_{+1} + \vec{E}_{-1}|^2 = A_0^2 + 2A_1^2 + 2A_1^2 \cos(2kx \sin\theta) + 4A_0A_1 \cos(kx \sin\theta)\cos[2kz \sin^2(\theta/2)], \quad (6)$$

where A_0, A_1 are the amplitudes of 0th and ±1st order beams, respectively, k is the amplitude of wave vector, and θ is the incident angle of ±1st order beams.

In Eq. (6), there is a z dependence in "cos" term, which means that the imaging plane must be limited in some focus range to form a good image. It is the origin of depth of focus.

The simulation results of three-beam interference with 200 nm and 1 μm size bubble under TE illumination are shown in Figs. 7(b) and 7(c). The intensity of three beams was set equal. As compared with the situation with no bubble as shown in Fig. 7(a), the resultant image is found to interfere with the scattered light and resulted in image defect in the presence of bubbles. From the observation of Figs. 5 and 7, it is found that when more beams are involved in the image formation, more scattered waves appear, interfering with the image forming light and contributing to the resultant image.

D. Scattering effect of moving bubbles

The water flows parallel to the resist surface during the water dispensing process. Therefore, there is a possibility for the bubbles moving parallel to the resist surface during the exposure process. To simulate the bubble moving effects, the following conditions are assumed: the repetition rate of the laser is 4 kHz; the pulse energy density on the wafer is 0.2 mJ/cm^2 per pulse; the resist sensitivity is 20 mJ/cm^2. The exposure time would be around 0.025 s to have enough dosage. In our FDTD simulation, the time interval of each time step was on the order of 10^{-17} s. To simulate the whole dynamic progress, we need at lease 10^{15} time steps, which is not possible in the simulation. Because the resist records the light intensity instead of the electrical field, we computed the scattering effects of the bubble statically at each sampling position along its moving path and then summed up all the intensity fields incoherently. Figure 8 shows the scattering effects of the 1 μm bubble with the moving distance of 1–4 μm during the exposure, which is equivalent to the moving speed of 40–160 μm/s. The scattering effect of the moving bubble was found to be averaged out when the moving speed is equal or larger than 160 μm/s. However, the flare introduced by the scattering may still contribute to the image background.

E. Three-dimensional FDTD simulation

Three-dimensional (3D) FDTD simulation on the scattering effects of one bubble is also carried out. Figure 9(a) shows the cross-section intensity distribution of a 1 μm bubble under TE-polarized two-beam illumination with an incident angle of 12°. The intensity distribution is similar as compared with the 2D-FDTD simulation in the middle picture of Fig. 5(d). Therefore, it is a good estimation for us to use 2D-FDTD for predicting the bubble scattering effects to save plenty of time. Figures 9(b)–9(d) show the images taken 0, 2.4, and 4.8 μm farther away from the bubbles, respectively. As the bubble sitting directly on the resist surface, deep circle shadow is observed below the position of the bubble. Strong interference between the scattered waves and imaging forming light appears around the shadow. When the

bubble moving away from the resist, the shadow gradually becomes weak and separates apart from center due to the two-beams illumination. The image is modulated and distorted by the scattered waves.

Moreover, the scattering effect of 60 nm bubble was also simulated by the 3D-FDTD technique. The image tangential to the last surface of the bubble is shown in Fig. 9(e). The center of the image is barely interfered by the scattered waves and gives little impact on the final resist image. This confirms again our previous prediction in Mie theory and 2D-FDTD simulation.

V. CONCLUSION

Air bubble scattering may pose a serious concern in immersion lithography. From a simple model, we show that no bubble can exist if its diameter is less than 7 nm. In the Mie analysis, scattering behavior of bubbles with various sizes was explored. The influence range of bubbles both in forward and lateral directions with respect to their size was analyzed. Together with the simulation from FDTD, it is predicted that as the bubble size exceeds 90 nm in diameter, light scattering becomes significant. When the bubble is sitting directly on the resist, the influence on the image is the most serious. The influence of the scattered waves tends to go deeper in the forward direction rather than to spread wider in the lateral direction. In the FDTD simulation, the interferences of scattered waves with two- and three-beam illuminations were simulated to mimic the actual imaging formation in an immersion scanner. It is found that the more beams are involved in the image formation, the more scattered waves would interfere with the image forming light and then contribute to the final image. The effect of the moving bubble was also simulated. If the moving speed of the 1 μm bubble is larger than 160 μm/s in our simulating condition of 0.025 s exposure time, the scattering phenomenon can be averaged out.

ACKNOWLEDGMENTS

The authors are grateful for the support from Taiwan Semiconductor Manufacturing Company under Contract No. 92-FS-B02, and in part by the National Science Council in Taiwan, Republic of China under Contract No. NSC 93-2218-E-002-018, and the computing support from the National Center for High-Performance Computing. Special thanks are due to K. Y. Chi and S. K. Liu for their helpful discussion.

[1]http://www.itrs.net/Common/2004Update/2004Update.htm
[2]B. J. Lin, J. Microlithogr., Microfabr., Microsyst. **3**, 377 (2004).
[3]S. Owa and H. Nagasaka, J. Microlithogr., Microfabr., Microsyst. **3**, 97 (2004).
[4]M. Switkes, R. R. Kunz, M. Rothschild, R. F. Sinta, M. Yeung, and S.-Y. Baek, J. Vac. Sci. Technol. B **21**, 2794 (2003).
[5]M. Switkes, T. M. Bloomstein, R. R. Kunz, M. Rothschild, J. W. Ruberti, T. A. Shedd, and M. Yeung, Proc. SPIE **5377**, 469 (2004).
[6]T. S. Gau, C. K. Chen, and B. J. Lin, J. Microlithogr., Microfabr., Microsyst. **3**, 61 (2004).
[7]D. Gil and T. Brunner, Microlithogr. World (2005).
[8]L. A. Wang, W. C. Chang, K. Y. Chi, S. K. Liu, and C. D. Lee, Proc. SPIE **5720**, 94 (2005).
[9]M. W. Zemansky and R. H. Dittman, *Heat and Thermaldynamics* (McGill Hill, Singapore, 1981).
[10]L. S. Tong, *Boiling Heat Transfer and Two-Phase Flow* (Wiley, New York, 1965).
[11]C. F. Bohren and D. R. Huffman, *Absorption and Scattering of Light by Small Particles* (Wiley, New York, 1983).
[12]D. M. Sullivan, *Electromagnetic Simulation Using the FDTD Method* (IEEE, New York, 2000).

Analysis of cladding-mode couplings for a lensed fiber integrated with a long-period fiber grating by use of the beam-propagation method

Wen-Yueh Su, Gia-Wei Chern, and Lon A. Wang

The beam-propagation method (BPM) is employed to analyze the coupling behavior of our scheme proposed previously, which combines a lensed fiber and a long-period fiber grating (LPFG) [Chen and Wang, Appl. Opt. **39,** 4490–4500 (2000)]. The influences of a core within the fiber lens are investigated. As for the fiber dependence of our coupling scheme, two typical fibers are studied: dispersion-shifted and single-mode, step-index fibers. With the BPM, the optimal coupling efficiencies for various source waists with corresponding lens radii and working distances are determined. We also compare the results with those obtained by use of the *ABCD* method and found that the BPM gives better agreement with experimental results. © 2002 Optical Society of America

OCIS codes: 060.2310, 050.2770, 230.7370.

1. Introduction

Efficient coupling of light from a laser diode (LD) to a single-mode fiber (SMF) plays an important role in optical fiber communication systems. The utilization of a lensed fiber provides desirable features such as being compact, stable, economical, and scalable to array-to-array coupling.[1–6] However, optical feedbacks from the lensed fiber end face severely affect the operation of an LD, e.g., output power, dynamic properties, and emission spectra, and it has been shown that a long working distance between LD and fiber can reduce the effective reflectivity.[7] Coupling schemes with a long working distance and that use an expanded-core fiber[8] or a graded-index fiber were proposed.[9,10] Recently, Chen and Wang[11,12] have demonstrated a new coupling method to obtain long working distances by utilizing a lensed fiber integrated with a long-period fiber grating (LPFG). In the scheme proposed here, light from an LD excites the fiber cladding mode that is then transferred into a fundamental core mode by the LPFG. Instead of coupling by the core mode, the cladding-mode field has a larger numerical aperture that enables efficient coupling at a long working distance.

An LPFG is an important all-fiber band rejection filter.[13] Resonant power transfer between core and cladding modes takes place when the phase-matching condition is satisfied. With a properly chosen grating period, resonant coupling at a given wavelength between core and specific cladding mode can be realized. Fiber cladding modes are confined by the cladding–air interface, and the corresponding mode fields extend over the cladding region.[14] Because of the larger cladding-mode radii, it is possible to realize couplings with long working distances by launching light into the cladding modes. Since the fiber cladding modes are linearly polarized[14] and have real-valued field distributions over the transverse plane, to have the larger excitation efficiency it is necessary to introduce a lensed fiber to compensate the curvature of the incident beam. With the properly chosen radii of the fiber lenses, coupling efficiencies of 78% and 35% at working distances 250 and 110 μm were demonstrated for fiber-to-fiber and LD-to-fiber couplings, respectively.[12]

Although the properties of cladding-mode couplings can be analyzed with the *ABCD* ray optics model,[12] the effects of fiber core cannot be properly taken into account. In this research, we use the beam-propagation method (BPM)[15,16] to investigate the field evolution through the lensed fiber with and without a core. The BPM is a powerful technique for analyzing the wave propagation characteristics in a

The authors are with the Department of Electrical Engineering and Institute of Electro-Optical Engineering, National Taiwan University, Taipei, Taiwan. L. A. Wang's e-mail address is lon@ccms.ntu.edu.tw.

Received 3 April 2002.
0003-6935/02/316576-09$15.00/0

wide variety of inhomogeneous media,[17–19] including the design of lensed fiber coupling.[10,16] Through the BPM analysis, we examine the transformation of the electric field when the incident beam propagates into the fiber lens. The dependence of mode excitation efficiencies on fiber cores is also studied.

This paper is organized as follows. In Section 2, the proposed scheme is reviewed, and the *ABCD* matrix method is outlined. We highlight the BPM to be employed for the analysis of the lensed fiber. A mode-expansion method is then used to calculate the coupling efficiency. In Section 3, the behavior of cladding-mode coupling is found to depend significantly on the size of the initial waist. For two exemplary initial waists, we compare the results among those obtained by the *ABCD* method, the BPM, and the measured ones. We also discuss their deviations from one another. The fiber dependence of the proposed coupling scheme and the limitation of the waist of the light source used for coupling are also studied. Section 4 concludes this study.

2. Two Analysis Methods

The working principle of the LPFG-assisted fiber coupling has been reported previously.[11,12] In the scheme proposed here, the first cladding mode of an SMF is to be optimized to have the high excitation efficiency for an incident Gaussian beam. The excited cladding mode is then coupled to the fundamental core mode by an LPFG. To enhance the excitation efficiency, the fiber end should be properly shaped to compensate the curvature of the incident beam. A simple lensed fiber is used for this purpose.[11] Although the use of *ABCD* matrix method is straightforward and leads to a qualitative agreement with the experimental results for calculating coupling efficiency,[12] the effects of the core region, the actual shape of fiber lens, and the radiation loss cannot be properly considered. In the following, we shall use the BPM to compare field evolution and mode excitation of a fiber lens with and without a fiber core. A mode-expansion method is then used to calculate the excitation efficiency of the corresponding modes after propagation through the lens.

A. Analytic Approach Based on the *ABCD* Method

A schematic coupling diagram is shown in Fig. 1. A laser source in plane $Z = Z_1$ has the Gaussian beam parameters of waist $W_1 = W_0$ and curvature $R_1 = \infty$. After propagation through a working distance Z_s, the beam parameters become

$$W_2 = W_0\left[1 + \left(\frac{Z_s}{Z_0}\right)^2\right]^{1/2}, \tag{1}$$

$$R_2 = Z_s\left[1 + \left(\frac{Z_0}{Z_s}\right)^2\right], \tag{2}$$

where $Z_0 = n_1\pi {W_0}^2/\lambda_0$ is the Rayleigh parameter; n_1 is the refractive index in region I; and λ_0 is the operating wavelength. W_2 and R_2 are the new parameters in plane Z_2, i.e., the front end plane of the fiber

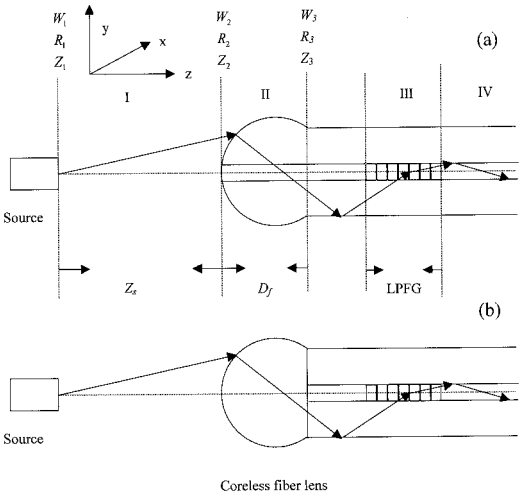

Fig. 1. Schematic diagrams of the coupling scheme studied in the text for (a) a cored fiber lens and (b) a coreless fiber lens integrated with an LPFG. Abbreviations are defined throughout the text.

lens. At normal incidence, the composite *ABCD* matrix after the beam propagating through the lens and a free distance D_f is

$$\mathbf{M} = \begin{bmatrix} A & B \\ C & D \end{bmatrix} = \begin{bmatrix} 1 + D_f\dfrac{n_1 - n_2}{n_2 R_f} & D_f\dfrac{n_1}{n_2} \\ \dfrac{n_1 - n_2}{n_2 R_f} & \dfrac{n_1}{n_2} \end{bmatrix}, \tag{3}$$

where R_f is the radius of the lens and n_2 is the refractive index in region II. The transformed beam parameters in plane Z_3 before the LPFG then become

$$W_3 = W_2\left[\left(A + \frac{B}{R_2}\right)^2 + \left(\frac{\lambda_0 B}{\pi {W_2}^2}\right)^2\right]^{1/2}, \tag{4}$$

$$R_3 = \frac{\left(A + \dfrac{B}{R_2}\right)^2 + \left(\dfrac{\lambda_0 B}{\pi {W_2}^2}\right)^2}{\left(A + \dfrac{B}{R_2}\right)\left(C + \dfrac{D}{R_2}\right) + BD\left(\dfrac{\lambda_0}{\pi {W_2}^2}\right)^2}. \tag{5}$$

Assume that the incident Gaussian beam is linearly polarized and that the normalized electric field in plane $Z = Z_3$ can be expressed

$$\mathbf{E}_3 \cong \hat{\mathbf{y}} E_{3,y} = \hat{\mathbf{y}}\left(\frac{1}{\pi {W_3}^2}\right)^{1/2} \exp\left(-\frac{r^2}{{W_3}^2} - \frac{ik_1 r^2}{2R_3}\right), \tag{6}$$

where $r = (x^2 + y^2)^{1/2}$ is the radial distance and $k_1 = n_2 2\pi/\lambda_0$. This field will be used in the following mode-expansion analysis for computing the mode excitation efficiency.

B. Numerical Approach Based on the Wide-Angle Beam Propagation Method

Here we apply the BPM to investigating field evolution in the fiber lens so that the effects of the finite

cladding radius and the existence of fiber core can be properly taken into account. Because both the core and the cladding modes under consideration are almost linearly polarized,[14] the electrical field with azimuthal order l can be expressed

$$\mathbf{E}(r, \phi, z) = \hat{\mathbf{y}}\psi(r, z)\exp(-ikn_a z)\exp(il\phi), \quad (7)$$

where n_a is the properly chosen reference refractive index and k is the wave number in free space. In the following, we consider a circularly symmetric guiding structure, i.e., $n = n(r, z)$. The scalar field ψ satisfies the following wave equation

$$2ikn_a \frac{\partial\psi}{\partial z} - \frac{\partial^2\psi}{\partial z^2} = \frac{\partial^2\psi}{\partial r^2} + \frac{1}{r}\frac{\partial\psi}{\partial r} - \frac{l^2}{r^2} + k^2(n^2 - {n_a}^2)\psi = \mathbf{H}\psi, \quad (8)$$

where $\mathbf{H}$ is the corresponding finite-difference matrix. The corresponding matrix elements can be found in, e.g., Ref. 17 A (1, 1) Padé approximation is used to derive the following equation[19]:

$$\frac{\partial\psi}{\partial z} = \frac{-i(\mathbf{H}/2kn_a)}{1 + (\mathbf{H}/4k^2{n_a}^2)}\psi. \quad (9)$$

By discretizing the nonuniform guiding structure into a stepwise one and using the finite-difference scheme, one can integrate Eq. (9) to give

$$\left(1 + \frac{1 + ikn_a\Delta z}{4k^2{n_a}^2}\mathbf{H}\right)\psi(z + \Delta z) = \left(1 + \frac{1 - ikn_a\Delta z}{4k^2{n_a}^2}\mathbf{H}\right)\psi(z). \quad (10)$$

With the initial condition $\psi(z = Z_2) = E_2$, the field evolution through the fiber lens can thus be obtained. Since the field under consideration has a wide extension along the radial distance, to prevent artificial reflections from the window boundary, it is necessary to employ a transparent boundary condition.[20]

Again, let $\mathbf{E}_3$ be the field after propagating through the lens and the mode-expansion method be used to calculate the excitation efficiency. The guided modes with circular symmetry are the LP_{0m} modes, with $m = 1$ corresponding to the core mode and $m > 1$ corresponding to cladding modes. Let $\mathbf{e}_{0m}$ be the LP_{0m} mode field that is normalized to carry 1-W optical power. With the orthogonality relation, the field $\mathbf{E}_3$ can be expanded as

$$\mathbf{E}_3 = \sum_m \mathbf{E}_{0m} + \mathbf{E}_{\text{rad}} = \sum_m a_m\mathbf{e}_{0m} + \mathbf{E}_{\text{rad}}, \quad (11)$$

where $\mathbf{E}_{0m}$ is the field projection in mode LP_{0m} and $\mathbf{E}_{\text{rad}}$ represents the unconfined radiation modes. The excitation efficiency of mode LP_{0m} is the ratio of power carried by this mode to the incident power. By normalizing the incident field $\mathbf{E}_0$ to carry power 1 W, the overall excitation efficiency of mode LP_{0m} is then given by

$$\eta_{0m} = \left|\iint \mathbf{E}_3 \cdot \mathbf{e}_{0m}^* dA\right|^2 = |a_m|^2. \quad (12)$$

The total coupling efficiency at wavelength λ can thus be expressed with the excitation efficiencies and the transmission of the LPFG as

$$\eta_{\text{total}} = \frac{\int\left[\eta_{01}(\lambda)T_{01}(\lambda) + \sum_{m=2,3,\ldots}\eta_{0m}(\lambda)T_{0m\to01}(\lambda)\right]P(\lambda)d\lambda}{\int P(\lambda)d\lambda}, \quad (13)$$

where $T_{01}(\lambda)$ is the self-transmission of core mode through LPFG at wavelength λ and $T_{0m\to01}(\lambda)$ for $m = 2, 3, \ldots$ is the cross transmission of LPFG from cladding mode LP_{0m} to core mode at wavelength λ. $P(\lambda)$ is the spectral power distribution of source. For a practical design, the grating period is adjusted to obtain the resonance between the fundamental core mode (LP_{01}) and the first cladding mode (LP_{02}) at the source wavelength. Assume the source beam is monochromatic at λ_0, then the total coupling efficiency can be approximated by

$$\eta_{\text{total}} \cong [1 - L(\lambda_0)]{\eta_{01}}^{\text{co}} + L(\lambda_0){\eta_{02}}^{\text{cl}}, \quad (14)$$

where $L(\lambda_0)$ is the loss of LPFG at λ_0, i.e., $L \cong 1 - T_{01} = T_{02\to01}$. Here we assume the resonance between the core and the first cladding modes is ideal, i.e., the energy of the first cladding mode can be completely transferred into the core mode by an LPFG. From Eq. (14), it can be seen that to have a large coupling efficiency, $L(\lambda_0)$ should be equal to 1, and the total efficiency is the excitation efficiency of the first cladding mode.

3. Results and Discussion

By using the BPM, one can study in detail the transformation of the electric field within the fiber lens. In the following, therefore, we shall first compare the field evolution within a fiber lens with and without a core. Specifically, we shall use the BPM to investigate the influences of the existence of a core on mode excitations and coupling efficiencies. Then we shall study the effects of a core region on the coupling behavior. For the fiber dependence of our coupling scheme, two typical fibers are considered, one is the standard SMF with step-index (SI) profile, and the other is a dispersion-shifted fiber (DSF), as used in our experiment. We also study the dependence of coupling efficiency on the initial waist of source. The results with the BPM are compared with those from the *ABCD* method and from the experiment reported previously.[11,12] Note that two kinds of light sources are used. The first is for fiber-to-fiber cou-

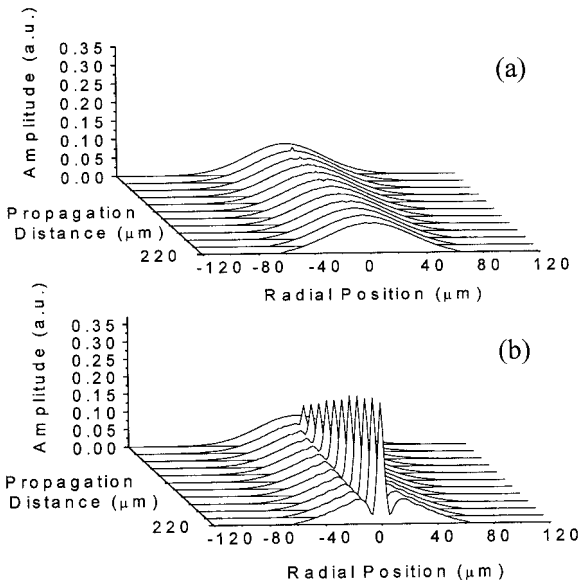

Fig. 2. Evolution of a Gaussian beam through (a) the coreless lens and (b) the cored lens from the source beam with an initial waist of 3.25 μm and at a working distance of 250 μm.

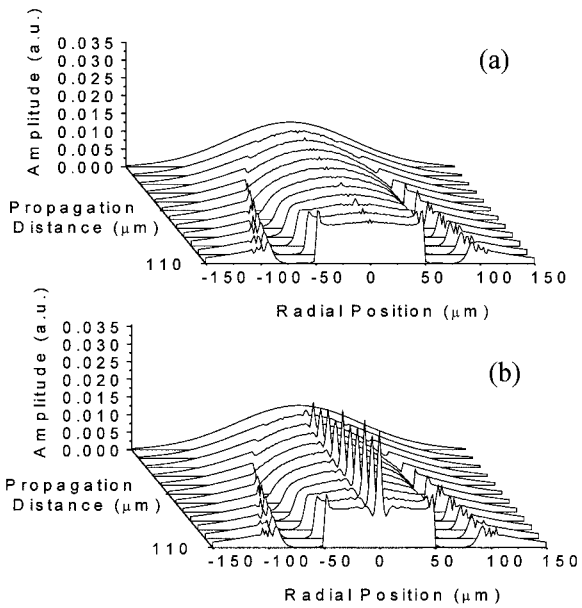

Fig. 3. Evolution of a Gaussian beam through (a) the coreless lens and (b) the cored lens from the source beam with an initial waist of 1 μm and at a working distance of 160 μm.

pling, which resembles a source with a large waist. The second is for LD-to-fiber coupling in which the source is Fabry–Perot laser diode.

A. Analysis of the Coupling Scheme

Two types of fiber lens structures with and without a core, as shown in Fig. 1, are considered. The source wavelength is 1.56 μm. To study the effects of the coupling behavior on the beam waists, we consider two beam waists 3.25 and 1 μm, exemplifying large and small waists, respectively. The radii of the fiber lens are $R_f = 120$ μm for coupling the 3.25-μm-waist source and $R_f = 75$ μm for the 1-μm-waist source. The numerical window size in the BPM simulation is 300 μm, and the number of grids is 1000, corresponding to a $\Delta r = 0.3$ μm. The step size (Δz) ranges from 0.025 to 0.2 μm from the consideration of required accuracy and numerical stability. The evolution of the field amplitude through the fiber lens is shown in Fig. 2 for the coupling of the 3.25-μm-waist source. The working distance Z_s is 250 μm, and the step size is chosen to be $\Delta z = 0.025$ μm. Figure 2(a) shows the transformation of an incident Gaussian beam in a coreless lens, whereas Fig. 2(b) corresponds to a cored DSF lens. Since the divergence angle of the Gaussian beam from the source is small (~8.75° in half-angle), there is not much beam truncation owing to the finite lens size. For the coreless case as shown in Fig. 2(a), the transformation of the incident Gaussian beam should be close to that simulated by use of the *ABCD* method, which will be illustrated [see Fig. 5(a) below]. Because of the small amplitude at the cladding boundaries, the reflection from the cladding–air interface is not significant. However, the multiple reflection of field at the core–cladding interface induces a central peak in the core region as shown in Fig. 2(b). At the end of the cored-fiber lens, the field amplitude has a narrow peak in the central part and a dip at $r = \pm 6.6$ μm. By projecting the transformed field in the various guided modes, the field is found to be composed mainly of modes ~8.6% LP_{01} and ~83% LP_{02}.

Figure 3 shows the corresponding field evolution through a fiber lens for the coupling of the small-waist source. The coreless case is shown in Fig. 3(a), whereas the case with a DSF core is shown in Fig. 3(b). The working distance Z_s is 160 μm and the step size is set the same as that in Fig. 2. Since the divergence angle of the source is ~28.45° in half-angle and the incident beam size is large compared with the lens diameter, the amplitude of electric field at the cladding–air interface is still large and will be reflected. It can be seen from Fig. 3 that the incident Gaussian beam is truncated by the lens boundary and that partial energy is reflected from the cladding–air interface. The reflected field then interferes with the outgoing components. This interference causes an oscillation in the dependence of coupling efficiency on the working distance [see Fig. 5(b) below]. In Fig. 3(b), an extra peak results in the central region owing to the existence of a DSF core.

Since the coupling efficiency depends on the excitation efficiencies of the core (LP_{01}) and the first cladding (LP_{02}) modes, it would be useful to study the evolution of fraction of power in local guiding modes (LP_{01} and LP_{02}) of the lens with a DSF core. The local guiding structure has a cladding radius defined by $R(z) = [R_f^2 - (R_f - z)^2]^{1/2}$, and the local modes are solved from the corresponding local guiding structure by use of the finite-difference method. In Fig. 4, we show the evolution of coupled power in local modes for the coupling from 3.25- and 1-μm-waist sources. In both cases, the fraction of power in the local core

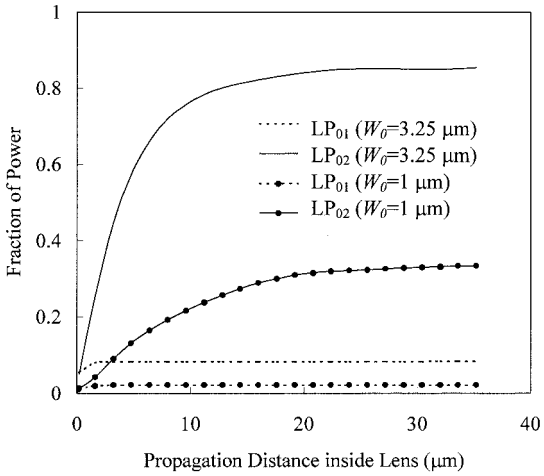

Fig. 4. Fraction of power in local modes LP_{01} and LP_{02} as a function of the propagation distance inside lens. The zero point of the propagation distance corresponds to the entrance of lens.

mode is small (less than 0.1) and remains nearly a constant as the field propagates inside the lens. On the other hand, the fraction of power in local cladding mode increases monotonically and saturates at distances greater than 30 μm. The coupled fractional power in the local mode LP_{02} saturates at ~83% for coupling the 3.25-μm-waist and ~31% for the 1-μm-waist sources.

The calculated coupling efficiency versus the working distance for couplings from a 3.25-μm-waist source, obtained with Eq. (14), is shown in Fig. 5(a). When an ideal transmission LPFG is used, the coupling efficiency is equal to the excitation efficiency of the cladding mode LP_{02}. Three curves are shown in Fig. 5(a), corresponding to the results simulated with and without a fiber core by the BPM and by the *ABCD* method. The maximum coupling efficiencies are found to be approximately 83%, 84%, and 86% at Z_s = 250 μm. The estimated corresponding longitudinal tolerances at a 1-dB loss are found to be approximately 60 μm for all the three cases. Similar coupling behaviors for a lensed fiber with and without a core indicates that the proposed scheme does not depend on the existence of a core. Although the field evolution is significantly influenced by the existence of the fiber core, as shown in Figs. 2 and 3, the cladding-mode excitation efficiency is insensitive to the existence of the core. This can be understood as follows. Let $E_y^{(a)}$ and $E_y^{(b)}$ be the transformed electric fields for the lens structure with and without the core, respectively, in plane Z_3 with the same input field. For example, $E_y^{(a)}$ and $E_y^{(b)}$ are fields in Figs. 2(a) and 2(b) at the propagation distance of 220 μm. The extra field due to the presence of core is the difference of these two fields, i.e., $E_{\text{diff}} = E_y^{(b)} - E_y^{(a)}$. In Fig. 6, we show the amplitude of the difference field E_{diff}, and the phase is shown in the inset. The projections of this difference field into LP_{01} and LP_{02} modes are 0.96 and 0.0007, respectively. It means that the difference field is quite similar to the core mode and

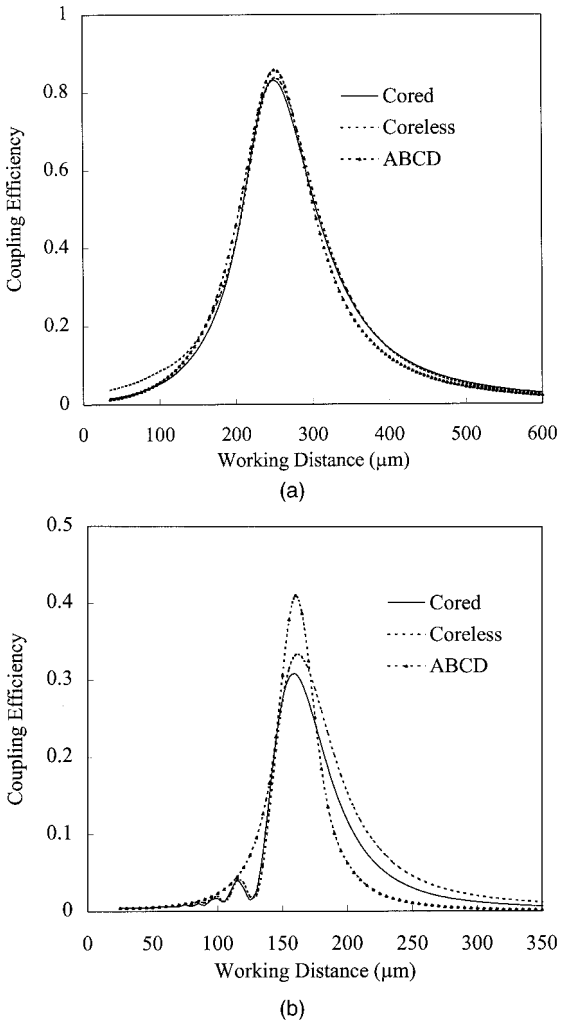

Fig. 5. Calculated coupling efficiencies versus the working distance by use of the BPM (cored and coreless lens) and by use of the *ABCD* method for couplings from the source (a) with an initial waist of 3.25 μm and (b) with an initial waist of 1 μm.

almost orthogonal to the first cladding mode. The small overlapping with the cladding mode LP_{02} indicates that the extra field induced by a core contributes negligibly to the coupling efficiency, because the proposed coupling scheme is dominated by the first cladding-mode excitations. The calculated coupling efficiency by the BPM is also close to the result of the *ABCD* method. For the case of large-waist source, therefore, the coupling efficiency can well be simulated with the *ABCD* method.

Figure 5(b) shows the coupling efficiencies versus the working distance for coupling a 1-μm-waist source. The maximum coupling efficiencies are found to be approximately 31%, 33%, and 41% at Z_s = 160 μm for the cored-lens, the coreless lens (from the BPM), and the *ABCD* method, respectively, and the estimated corresponding longitudinal tolerances at a 1-dB loss are found to be approximately 30, 35, and 20 μm, respectively. For small-waist sources, the divergence angle of the beam is large. Significant reflection occurs at the

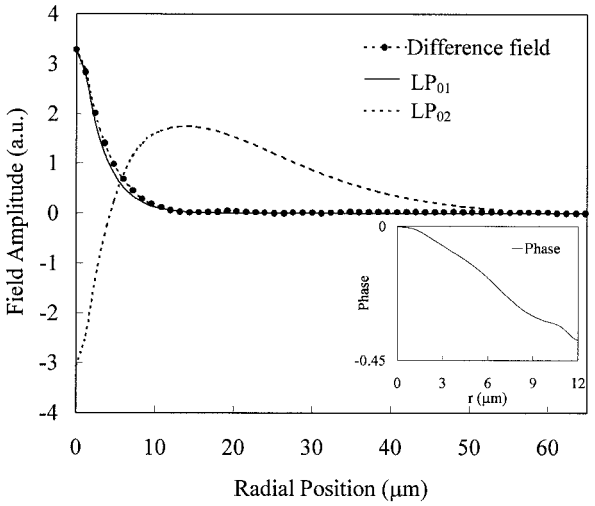

Fig. 6. Amplitude of the difference field E_{diff}, which is defined in the text and also compared with the electric field of modes LP_{01} and LP_{02}. The inset shows the phase of the difference field and the radial position is denoted as r.

cladding–air interface and manifests itself in an oscillating behavior in the coupling efficiency over the working distance owing to interference. Note that such an effect cannot be taken care of properly by use of the *ABCD* method.

Figure 7(a) shows the calculated coupling efficiencies versus the working distances for fiber-to-fiber coupling, and the measured data taken from the previous work[11,12] are included. The source beam waist is chosen to be 3.25 μm, corresponding to the beam waist of the core mode, and the lens radius is 120 μm. The maximum coupling efficiency is ~78% at a working distance of 250 μm, and the coupling efficiency has a longitudinal tolerance of ~60 μm at a 1-dB loss. The measured coupling efficiencies are larger than the calculated ones in the short working distance, which can be attributed to the reduced transmission loss of LPFG. The excited energy in LP_{01} mode is relatively large in short working distances. From Eq. (14), when $L(\lambda_0)$ is not equal to 1, both core (LP_{01}) and first cladding (LP_{02}) modes contribute to the coupling efficiency. As a result, the measured coupling efficiencies are larger. The possible reasons for the reduced transmission loss are the wavelength mismatch and the induced bending that also causes the resonant peak of the LPFG to shift during the assembly of the LPFG. Figure 7(b) shows the calculated coupling efficiencies versus the working distances for LD-to-fiber coupling with a lens radius of 75 μm. The previous reported data are included for comparison.[11,12] The maximum coupling efficiency is ~26% at a working distance of 160 μm for LD-to-fiber coupling, and the coupling efficiency has a longitudinal tolerance of ~50 μm at a 1-dB loss. The LD's beam profile has an ellipticity of 2.5 and the near-field beam waists are estimated to be 0.71 and 1.78 μm in the vertical and the parallel directions, respectively. For a general noncircularly symmetric input beam,

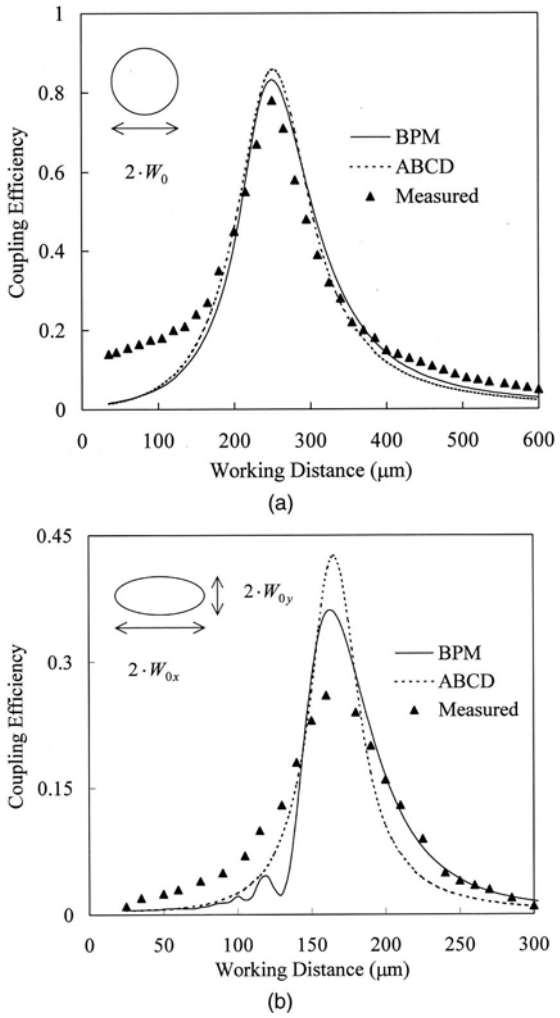

Fig. 7. Measured coupling efficiencies versus the working distance for (a) fiber-to-fiber coupling, where W_0 = 3.25 μm with a lens radius of 120 μm and (b) LD-to-fiber coupling, where W_{0x} = 1.78 μm and W_{0y} = 0.71 μm with a lens radius of 75 μm. The results are also compared with the calculated ones by use of the BPM and by use of the *ABCD* method.

we may expand the field into summation of different azimuthal orders,

$$\mathbf{E} = \sum_{l=0,1,2,\ldots} \mathbf{E}_l \exp(il\phi), \tag{15}$$

where the lth component is given by the Fourier formula. Since the guiding structure of lensed fiber is circularly symmetric, it conserves the angular momentum of the incident beam. Consequently, each azimuthal order propagates independently. Because the cladding modes under consideration have $l = 0$, higher-order components cannot excite these guided modes. Here, we use the BPM with $l = 0$ to study the transformation of the zeroth-order component of the elliptical beam. But in the *ABCD* method the elliptical source is dealt with directly. The calculated maximum coupling efficiencies are approximately 32% and 43% at Z_s = 165 μm with the BPM and the *ABCD* method, respectively, and the

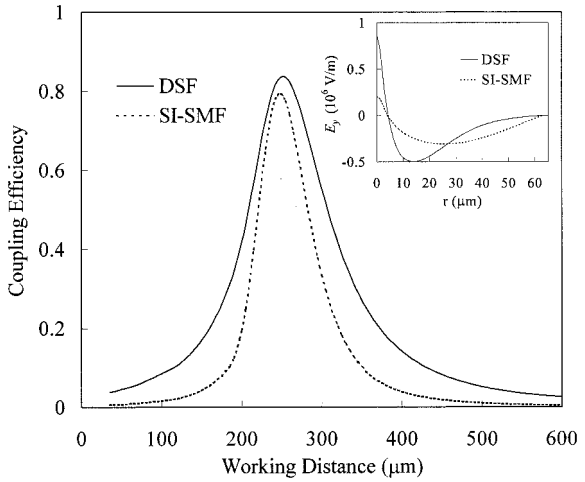

Fig. 8. Comparison of calculated coupling efficiencies of a DSF and an SI-SMF as a function of the working distance for couplings from a source with a 3.25-μm waist. The inset shows the field distribution for the first cladding modes of a DSF and an SI-SMF.

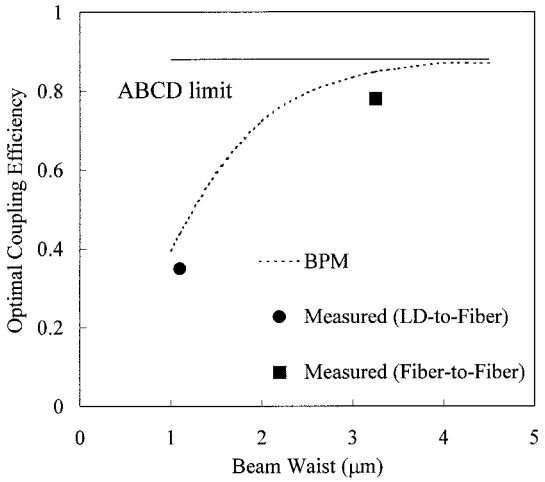

Fig. 9. Calculated and measured optimal coupling efficiency versus beam waist.

estimated corresponding longitudinal tolerances are approximately 30 and 20 μm, respectively. The measured coupling efficiencies in the short working distance are larger than the calculated ones for the same reason as described above. With the use of the BPM, the oscillating behavior in the calculated coupling efficiency over the working distance is attributed to the effect of the lens boundary as proved previously.

B. Fiber Dependence

Two fibers are considered: SMF and DSF. As discussed previously, the transmission loss of LPFG should be equal to 1 for the best coupling. From the coupled-mode theory, the transmission loss at resonance wavelength can be expressed

$$L = 1 - \cos^2(\kappa_{\text{co-cl}} l_g), \tag{16}$$

where l_g is the length of LPFG and $\kappa_{\text{co-cl}}$ is the coupling constant that has the following form,[14]

$$\kappa_{\text{co-cl}} = \frac{\omega \varepsilon_0 \Delta n_g}{2} \int_{A_{\text{co}}} n_{\text{co}} \mathbf{E}_{02} \cdot \mathbf{E}_{01}^* \mathrm{d}A, \tag{17}$$

where n_{co} is the refractive index of the fiber core and Δn_g is the index difference of the grating. Figure 8 shows the calculated coupling efficiencies versus the working distance for couplings from the 3.25-μm-waist source. The parameters used for calculation are the same as before. The inset shows the calculated electric field E_y for the first cladding modes (LP_{02}) of a DSF and an SI-SMF. With the field distributions of modes LP_{01} and LP_{02}, the coupling constants $\kappa_{\text{co-cl}}$ of the two kinds of fibers can be calculated with Eq. (17). If it is assumed that the photoinduced Δn_g is the same for both fibers, the coupling constant of DSF is ~3.6 times that of a SI fiber, which explains why the transmission loss of the first cladding mode of an SI-SMF is relatively small.

Assuming the same coupling constant, we compare the calculated coupling efficiency of a DSF to that of an SI-index SMF. The optimal working distance for the maximum coupling efficiency is at 250 μm, and the coupling efficiencies of a DSF are larger than those of an SI-SMF for all working distances with the maximum efficiencies of ~83% and ~79% for the DSF and the SI-SMF, respectively. The longitudinal tolerance are of ~60 μm for a DSF and ~40 μm for an SI-SMF.

C. Source-Waist Dependence

The initial waist of the source seriously affects the characteristics of the proposed coupling scheme, as is clearly demonstrated in previous sections. In this section, we shall investigate the dependence of optimal coupling efficiency on source waists. The optimal coupling takes place when the incident beam curvature is compensated by the lens,[12] and the transformed electric field can be expressed as $\mathbf{E}_3 = \exp(-r^2/{W_3}^2)$. The optimal beam waist for maximum overlapping with the LP_{02} cladding mode is $W_{3,\text{opt}} = 33.5$ μm, which gives a coupling efficiency of 88%. When the initial waist of the source W_0 and the optimal transformed field waist $W_{3,\text{opt}}$ are given, the optimal working distance Z_s can be determined from Eq. (4) and the optimal lens radius R_f, from Eq. (5). In Fig. 9, we show the calculated optimal efficiencies versus the beam waists by use of the BPM and the *ABCD* method. The corresponding optimal conditions of the lens radius and the working distance versus the beam waists by use of the BPM and the *ABCD* method are shown in Fig. 10. Two measured coupling efficiencies and their optimal conditions corresponding to the LD-to-fiber coupling and the fiber-to-fiber coupling[11,12] are also included in the figures. The optimal measured efficiency for the LD-to-fiber coupling is 35% for a 50-μm lens radius and a 110-μm working distance. For the fiber-to-fiber coupling, the optimal measured efficiency is 78% for a 120-μm lens radius and a 250-μm working dis-

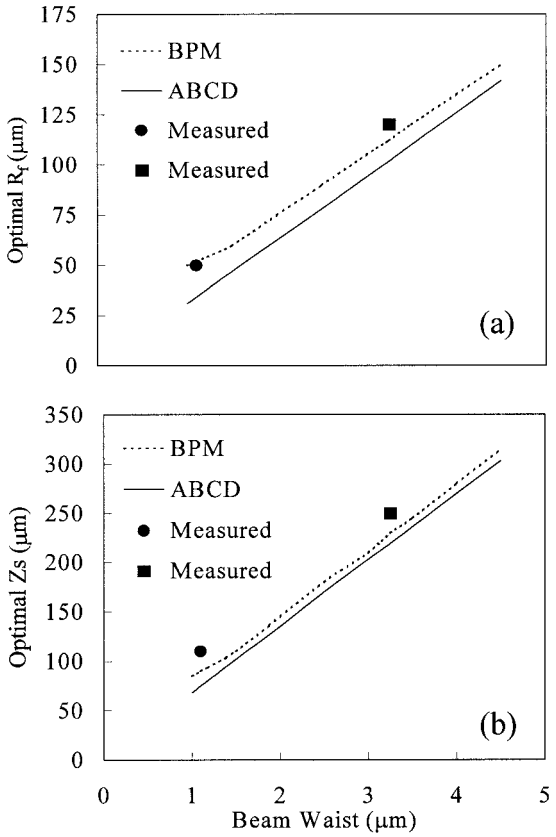

Fig. 10. Calculated and measured optimal conditions of (a) the lens radius (R_f) and (b) the working distance (Z_s) versus the beam waist. The measured one in the figures denoted as (●) is the case of LD-to-fiber coupling, and (■) is the case of fiber-to-fiber coupling.

tance. In Fig. 9, the optimal efficiency is a constant of ~88% for beam waists from 1 to 4.5 μm, with the *ABCD* method. However, the optimal coupling efficiency calculated from the BPM is only 40% for the source waist of 1 μm, and it monotonically increases with the waist and is saturated ~87% for the waist beyond 4 μm. With consideration of the finite aperture of a lensed fiber and of beam truncation, the simulated results based on the BPM are more consistent with the measured ones.

4. Conclusion

The BPM has been applied to the analysis of beam evolution through the fiber lens in the coupling scheme reported previously.[11,12] Since the effects of lens boundary and core cannot be properly accounted for in the *ABCD* method, the BPM is considered a better approach for the analysis. We consider two kinds of waist sizes 1-μm for the small-waist source and 3.25-μm for the large-waist source. From the BPM simulation, because of the large divergence angle, the incident beam from a small-waist source is truncated by the lens boundary, and partial energy is reflected from the interface. The reflected field then causes the oscillation of the coupling efficiency over the working distance. However, for the large-waist source, this effect is not significant. In addition, the existence of a fiber core has no significant effect on the coupling efficiency for the large- and the small-waist sources. Note for the large-waist source, efficiencies can reach as much as ~83% and 84% for the cored and coreless lenses, respectively. Also by our comparing the results from the BPM, the *ABCD* method is found quite applicable to such analysis if the source has a large waist.

The calculated coupling efficiencies versus working distances are compared with the experiment results, and an overall agreement is obtained. As for the fiber dependence of our coupling scheme, the coupling constant $\kappa_{co\text{-}cl}$ of a DSF is larger than that of an SI-SMF, which explains why the transmission loss of the first cladding mode of an SI-SMF, is small. By studying the coupling behavior of two kinds of fibers, it was found that the longitudinal tolerance for a DSF is also larger. The dependence of optimal coupling efficiencies on source beam waists shows that the BPM is more consistent with the measured efficiencies and that the larger beam waist would lead to a better optimal coupling efficiency.

The authors thank W. T. Chen for helpful discussions and experiment data. The authors are grateful for the support in part by the National Science Council Taiwan, under the contract NSC 90-2215-E-002-007 and by the Education Ministry under the contract 89-E-FA06-2-4 in Taiwan.

References

1. L. Cohen and M. Schneider, "Microlenses for coupling junction lasers to optical fibers," Appl. Opt. **13,** 89–94 (1974).
2. J. Yamada, Y. Murakami, J. Sakai, and T. Kimura, "Characteristics of a hemispherical microlens for coupling between a semiconductor laser and single-mode fiber," IEEE J. Quantum Electron. **QE-16,** 1067–1072 (1980).
3. H. Kuwahara, M. Sasaki, and N. Tokoyo, "Efficient coupling from semiconductor lasers into single-mode fibers with tapered hemispherical ends," Appl. Opt. **19,** 2578–2583 (1980).
4. K. S. Lee and F. S. Barnes, "Microlenses on the end of single-mode optical fibers for laser applications," Appl. Opt. **24,** 3134–3139 (1985).
5. K. Shiraishi, "New scheme of coupling from laser diodes to single-mode fibers: a beam expanding fiber with a hemispherical end," Opt. Lett. **29,** 3467–3469 (1990).
6. C. A. Edwards, H. M. Presby, and C. Dragone, "Ideal microlenses for laser to fiber coupling," J. Lightwave Technol. **11,** 252–257 (1993).
7. W. Bludau and R. Rossberg, "Characterization of laser-to-fiber coupling techniques by their optical feedback," Appl. Opt. **21,** 1933–1939 (1982).
8. K. Shiraishi, N. Oyama, K. Matsumura, I. Ohishi, and S. Suga, "A fiber lens with a long working distance for integrated coupling between laser diodes and single-mode fibers," J. Lightwave Technol. **13,** 1736–1744 (1995).
9. K. Shiraishi, H. Ohnuki, N. Hiraguri, K. Matsumura, I. Ohishi, H. Morichi, and H. Kazami, "A lensed-fiber coupling scheme utilizing a graded-index fiber and a hemispherically ended coreless fiber tip," J. Lightwave Technol. **15,** 356–363 (1997).
10. K. Shiraishi and S.-I. Kuroo, "A new lensed-fiber configuration employing cascaded GI-fiber chips," J. Lightwave Technol. **18,** 787–794 (2000).
11. W. T. Chen and L. A. Wang, "Laser-to-fiber coupling scheme by

utilizing a lensed fiber integrated with a long-period fiber grating," IEEE Photon. Technol. Lett. **12,** 501–503 (2000).
12. W. T. Chen and L. A. Wang, "Optical coupling method utilizing a lensed fiber integrated with a long-period fiber grating," Appl. Opt. **39,** 4490–4500 (2000).
13. A. M. Vengsarkar, P. J. Lemaire, J. B. Judkins, V. Bhatia, T. Erdogan, and J. Sipe, "Long-period fiber gratings as band-rejection filters," J. Lightwave Technol. **4,** 58–65 (1996).
14. T. Erdogan, "Cladding-mode resonances in short- and long-period fiber grating filters," J. Opt. Soc. Am. A **14,** 1760–1773 (1997).
15. M. D. Feit and J. A. Fleck, Jr., "Light propagation in graded-index optical fibers," Appl. Opt. **17,** 3990–3998 (1978).
16. B. Hermansson, D. Yevick, and J. Saijonmaa, "Propagation-beam-method analysis of two-dimensional microlenses and three-dimensional taper structures," J. Opt. Soc. Am. A **1,** 663–671 (1984).
17. F. Gonthier, A. Henault, S. Lacroix, R. J. Black, and J. Bures, "Mode coupling in nonuniform fibers: comparison between coupled-mode theory and finite-difference beam-propagation method simulations," J. Opt. Soc. Am. B **8,** 416–421 (1991).
18. J. P. Zhang and K. Petermann, "Beam propagation model for vertical-cavity surface-emitting lasers: threshold properties," IEEE J. Quantum. Electron. **30,** 1529–1536 (1994).
19. J. Yamauchi, Y. Akimoto, M. Nibe, and H. Nakano, "Wide-angle propagation analysis for circularly symmetric waveguides: comparison between FD-BPM and FD-TDM," IEEE Photon. Technol. Lett. **8,** 236–238 (1996).
20. G. R. Hadley, "Transparent boundary condition for beam propagation," Opt. Lett. **16,** 624–626 (1991).